

Super-Resolution for Multislice Diffusion Tensor Imaging

Dirk H. J. Poot,¹ Ben Jeurissen,² Yannick Bastiaensen,² Jelle Veraart,² Wim Van Hecke,^{2,3} Paul M. Parizel,³ and Jan Sijbers^{2*}

Diffusion weighted magnetic resonance images are often acquired with single shot multislice imaging sequences, because of their short scanning times and robustness to motion. To minimize noise and acquisition time, images are generally acquired with either anisotropic or isotropic low resolution voxels, which impedes subsequent posterior image processing and visualization. In this article, we propose a super-resolution method for diffusion weighted imaging that combines anisotropic multislice images to enhance the spatial resolution of diffusion tensor data. Each diffusion weighted image is reconstructed from a set of arbitrarily oriented images with a low through-plane resolution. The quality of the reconstructed diffusion weighted images was evaluated by diffusion tensor metrics and tractography. Experiments with simulated data, a hardware DTI phantom, as well as in vivo human brain data were conducted. Our results show a significant increase in spatial resolution of the diffusion tensor data while preserving high signal to noise ratio. Magn Reson Med 000:000–000, 2012. © 2012 Wiley Periodicals, Inc.

Key words: diffusion tensor magnetic resonance images; super-resolution; multislice imaging; reconstruction; multidimensional imaging

Diffusion tensor imaging (DTI) is a noninvasive, in vivo imaging modality that measures the diffusion of water molecules (1). During a DTI sequence, diffusion weighting gradients are applied to attenuate the signal when diffusion is present. As a result, the signal-to-noise ratio (SNR) of diffusion weighted (DW) images is relatively low (2). Furthermore, since DTI is sensitive to translational motion of water molecules, a small amount of subject motion can lead to phase shifts or signal loss. Because of their short measuring times and robustness to motion, multislice single shot echo planar imaging (3) or single shot fast spin echo (4,5) sequences are preferred for acquiring diffusion tensor (DT) data. Achieving high spatial resolution (HR) DW images with isotropic voxels and a high SNR with these sequences is a challenging task (6). Acquiring isotropic HR images directly leads to images with low SNR, as the recorded

signal energy scales linearly with the slice thickness. Lowering the resolution improves the SNR, but increases partial volume effects, which hinders visual interpretation and also impedes posterior fitting of the DT model (7).

As will be demonstrated in this article, the previously mentioned problems can be overcome by image processing/reconstruction methods that increase the spatial resolution by combining information from a number of images, termed super-resolution. For magnetic resonance images (MRIs), several super-resolution methods have been proposed. Peled and Yeshurun (8) and Carmi et al. (9) proposed to improve the in-plane resolution by combining multiple in-plane subpixel shifted MRIs. The validity of that approach was questioned by Scheffler (10), who argued that the shifted MR images are acquired at exactly the same k -space data points. Indeed, the in-plane shift only results in a linear phase shift, thus each shifted MRI contains the same information, except for measurement noise. Furthermore, the blurring due to the finite part of k -space was ignored and through-plane resolution was untouched. A more promising in-plane super-resolution technique based on modulating the magnetization has recently been published by Ropele et al. (11). Greenspan et al. (12), and Kornprobst et al. (13) improved the through-plane resolution by shifting the slice directions of multiple multislice acquisitions. The acquisition in the slice direction is not band limited, and therefore, the method is not limited to the original resolution. Reconstructions using multiple orthogonal sets with a high in-plane resolution and a lower through-plane resolution were performed by Gholipour et al. (14) and Rousseau et al. (15). Their work mainly focused on fetal brain images. The problem of fetal motion was addressed by an interslice registration-based reconstruction. Shilling et al. (16) described rotating non-isotropic low resolution (LR) multislice MRIs around a common frequency encoding axis to obtain a HR image. The reconstruction problem was stated as a set of linear equations from which a HR image was solved. The linear equations were resolved by iterative techniques also used in computed tomography (e.g. algebraic reconstruction technique). This method was extended by Poot et al. (17) to allow arbitrary slice orientations. In their work, the linear equations were solved with the conjugated gradient method and optimized affine transformations were used to apply the coordinate transformations. Both techniques substantially increased the performance of the algorithm.

For DTI data, only a limited number of super-resolution techniques were proposed. Jiang and Hsu (18) investigated procedures to adequately reconstruct reduced encoded DW images based on k -space sharing with a HR non-DW image.

¹Departments of Medical informatics and Radiology, BIGR, Erasmus Medical Center, Rotterdam, the Netherlands

²IBBT-Vision Lab, Department of Physics, Vision Lab, University of Antwerp, Antwerp, Belgium

³Department of Radiology, University Hospital Antwerp, University of Antwerp, Edegem (Antwerp), Belgium

Grant sponsor: Institute for the Promotion of Innovation through Science and Technology in Flanders (SBO-project Technology; IWT Vlaanderen); Grant number: 060819; Grant sponsor: IBBT SuperMRI project; Grant sponsor: Care4ME project (Agentschap NL under the ITEA2 program)

*Correspondence to: Jan Sijbers; Department of Physics, Vision Lab, University of Antwerp, Universiteitsplein 1, N 1.13, B-2610 Antwerp, Belgium. E-mail: jan.sijbers@ua.ac.be

Received 11 July 2011; revised 31 January 2012; accepted 7 February 2012.

DOI 10.1002/mrm.24233

Published online in Wiley Online Library (wileyonlinelibrary.com).

The reconstruction accuracy was improved by adding filtering to select for desired frequency information and by using baseline correction to maintain signal continuity between the reduced encoded data and reference data. Except for the criticized work by Peled and Yeshurun (8), to our knowledge, none of the previously mentioned magnetic resonance imaging superresolution methods were ever studied on DTI data, although more conventional in-plane resolution improvement techniques have been proposed, e.g. Ref. 19.

In this work, the method by Poot et al. (17) is extended to reconstruct an isotropic HR DTI image from a set of anisotropic multislice DTI images. The impact on SNR, acquisition time and artifacts of DW images will be investigated. Furthermore, the influence on DTI parameters like fractional anisotropy (FA), the first eigenvector (FE), and “whole brain” tractography is studied.

MATERIALS AND METHODS

Before explaining the super-resolution part of the method, the diffusion tensor model will be reviewed first.

Diffusion Tensor Model

The diffusion tensor \mathbf{D} is represented by a 3×3 symmetric, positive definite tensor, which is characterized by six unique components. Therefore, at least six DW images, with non collinear diffusion weighting gradient directions, are acquired to estimate \mathbf{D} . Let \mathbf{r}_m ($n_{r_m} \times 1$) denote the m th $\in \{1, \dots, M; M \geq 6\}$ DW image and \mathbf{x}_k , $k \in \{1, \dots, n_{r_m}\}$ the grid points of \mathbf{r}_m . Then, the noise free DW image intensity in each voxel k is modeled by:

$$\mathbf{r}_m(k) = \mathbf{r}_0(k) e^{-\mathbf{g}_k^T \mathbf{D}^{(k)} \mathbf{g}_m b_m}, \quad [1]$$

where \mathbf{g}_m and b_m are the diffusion gradient direction and diffusion weighting factor of the corresponding DW image \mathbf{r}_m , respectively, and \mathbf{r}_0 represents the non-DW signal. All DT are estimated from the DW images with a nonlinear maximum likelihood estimator, assuming Rician distributed noise (20).

Super-Resolution Model

The proposed method reconstructs each of the M HR DW images \mathbf{r}_m from N DW images with different slice directions, each with a low through-plane resolution. After reconstructing all M HR DW images, a diffusion tensor map [1] is estimated from these reconstructed HR DW images. Note that the acquisition of the multislice MRIs can be accelerated by any standard technique, such as parallel imaging (21,22), as long as the slice excitation profile and the in-plane point spread function exist and are known.

For the reconstruction method, the MR image acquisition process is implicitly splitted in two steps. First a continuous “image” with the desired contrast is created. This “image” is equal for all LR images with a specific m . The reconstruction process aims to reconstruct a HR sampled version of this image. Subsequently, N LR images are sampled from this image. This anisotropic sampling can be represented by a linear operator operating on the images

represented by vectors constructed from concatenating the intensities at all sampled locations. Thus, the acquisition of the j th $\in \{1, \dots, N\}$ slice direction image \mathbf{s}_{jm} ($n_{s_{jm}} \times 1$) is modeled as:

$$\mathbf{s}_{jm} = \mathbf{X}_j \mathbf{r}_m + \mathbf{e}_{jm}, \quad [2]$$

where \mathbf{e}_{jm} ($n_{s_{jm}} \times 1$) represents the measurement noise and \mathbf{X}_j ($n_{r_m} \times n_{s_{jm}}$) the projection matrix described as:

$$\mathbf{X}_j(l, k) = \omega(\mathbf{T}_j(\mathbf{x}_k) - \mathbf{y}_l), \quad [3]$$

where \mathbf{y}_l , $l \in \{1, \dots, n_{s_{jm}}\}$ is the coordinate in the space of the LR image \mathbf{s}_{jm} . The transformation \mathbf{T}_j transforms points in the object space, \mathbf{x}_k , to the space of the j th LR image, \mathbf{y}_l . These transformations typically consist of affine transformations, as both the grid of the HR reconstruction and the grid of the LR images is regular in physical space. However, more general transformations can be applied as well. The point spread function of the acquisition is represented by ω , which is defined by the MR image acquisition method. In case of a multislice acquisition, the sampling functions in read and phase direction are defined by a rectangular area in k -space that is sampled, thus, ω represents a Dirichlet or periodic sinc function. The through-plane sampling function is dependent on the slice selection profile, which is excited using a windowed sinc or a Gaussian shaped RF pulse. In this work, a windowed sinc RF pulse was used, so the slice excitation profile was modeled by a smoothed box function, as explained in Ref. 17.

If all N slice directions are combined, the acquisition model of a specific DW image m is given by:

$$\mathbf{s}_m = \mathbf{X} \mathbf{r}_m + \mathbf{e}_m, \quad [4]$$

with

$$\mathbf{s}_m = \begin{bmatrix} \mathbf{s}_{1m} \\ \vdots \\ \mathbf{s}_{Nm} \end{bmatrix}, \mathbf{X} = \begin{bmatrix} \mathbf{X}_1 \\ \vdots \\ \mathbf{X}_N \end{bmatrix}, \mathbf{e}_m = \begin{bmatrix} \mathbf{e}_{1m} \\ \vdots \\ \mathbf{e}_{Nm} \end{bmatrix}. \quad [5]$$

Reconstruction of the Object

The HR image \mathbf{r}_m can be estimated by minimizing the mean squared difference between \mathbf{s}_m and $\mathbf{X} \mathbf{r}_m$, which is a least squares problem:

$$\hat{\mathbf{r}} = \underset{\mathbf{r}}{\operatorname{argmin}} \|\mathbf{X} \mathbf{r} - \mathbf{s}\|_2^2. \quad [6]$$

where the index m is removed to simplify notation. The reconstruction process is performed for each m independently.

Because of the high resolution of the grid of the reconstructed object, this problem is badly conditioned or even underdetermined. Hence, regularization is required, leading to the following regularized least squares problem:

$$\hat{\mathbf{r}} = \underset{\mathbf{r}}{\operatorname{argmin}} \|\mathbf{X} \mathbf{r} - \mathbf{s}\|_2^2 + \lambda \mathbf{R}(\mathbf{r}), \quad [7]$$

where $\mathbf{R}(\mathbf{r})$ is a penalty function and λ a weighting factor. The choice for a regularization term in linear systems is still an active topic of research and also dependent on certain prior knowledge about the object to be reconstructed.

The HR grid generally contains spatial frequencies that are not sampled by any of the multislice images. Hence, since there is no information about these high spatial

frequencies, the regularization will be used to minimize the energy of these high frequencies. To this end, a regularization term is added that computes the squared laplacian of the reconstructed object:

$$\mathbf{R}(\mathbf{r}) = (\Delta \mathbf{r})^2 = \left(\frac{D^2 \mathbf{r}}{Dx^2} + \frac{D^2 \mathbf{r}}{Dy^2} + \frac{D^2 \mathbf{r}}{Dz^2} \right)^2. \quad [8]$$

The regularization is controlled by the weighting factor λ . Increasing λ increases the bias in the solution, while reducing the variance. A good value for λ would be a value that (approximately) minimizes the mean squared error (MSE). To solve the regularized least squares problem [7] the conjugate gradient method (23) was found to be adequate, because of its fast convergence properties.

As previously mentioned, the reconstruction problem is not only ill-posed, the system matrix \mathbf{X} is furthermore too large to be explicitly stored. If the transformation T [3] is an affine transform, the acquisition of the MRIs can be reformulated as an affine transform of the object, followed by the filter operations of the sampling functions described by ω . The affine transformations are applied with a transformation method developed by Poot et al. (17). The method decomposes the transformation into a set of shearlet transformations, providing very high quality resampling with relatively few computations.

Motion and Eddy Current Artefacts

Because of the long scan times required by DT experiments, non-negligible subject motion might be present in the DW data. Additionally, the slice direction data sets may contain (minor) eddy current artifacts and geometrical distortions due to B_0 inhomogeneity which is caused by magnetic susceptibility differences. These geometrical differences depend on the phase encoding direction and are therefore slice direction dependent (see Fig. 1). Furthermore, the alignment of the images using coefficients returned by the scanner was found to be insufficient for accurate reconstruction. Therefore, the coefficients of affine transforms needed to correct both the distortions and the incorrect alignment of images were calculated by minimizing the sum of squared residuals within a brain mask. Subsequently, the system matrix \mathbf{X} was corrected with these coefficients, followed

by the regularized least squares estimation. Note that the coefficients to correct eddy currents and motion artifacts are different for each LR DW image, while the corrections for magnetic susceptibility artifacts and misalignment of the scanner coefficients are the same for all LR DW images within the same slice orientation.

Experiments

To evaluate the proposed super-resolution reconstruction (SRR) method, simulation as well as phantom and in vivo DTI experiments were carried out.

DTI Simulated Phantom

First, experiments were run on simulated DTI phantom data. The phantom and the associated DW images were generated using the Numerical Fiber Generator software package (Brain Research Institute, Melbourne, Australia) (24). To simulate arbitrarily oriented slice direction images, HR DTI data was generated ($7 b = 0 \text{ s/mm}^2$ and $60 b = 1200 \text{ s/mm}^2$ images) with an image matrix of $160 \times 160 \times 160$. Subsequently, affine transformations were applied using eight optimally spread slice orientations, followed by the sampling filters described in the methods section. This resulted in eight differently rotated versions of the phantom data with image matrices of $40 \times 20 \times 10$. Optimal slice orientations were chosen based on an algorithm described by Jones et al. (25) for spreading out measurements in three-dimensional (3D) gradient vector space. Next, all images were corrupted with Rician noise. These eight simulated datasets were eventually used as inputs in the proposed SRR method to reconstruct one HR dataset with an image matrix of $40 \times 40 \times 40$. The number of iterations used in the conjugate gradient method was set to 15, which proved to be sufficient. Based on the MSE of the fractional anisotropy when using a phantom, more iterations resulted in a gain of less than 0,0001 per iteration.

The voxel volume of the simulated LR slices is eight times the volume of voxel of the HR image, implying that the theoretical scanning time of one slice oriented dataset will be eight times lower than that of a direct HR scan. Hence, the total scanning time of eight slice oriented datasets corresponds to that of a single HR acquisition. Note that, even though the scan time would be eight times

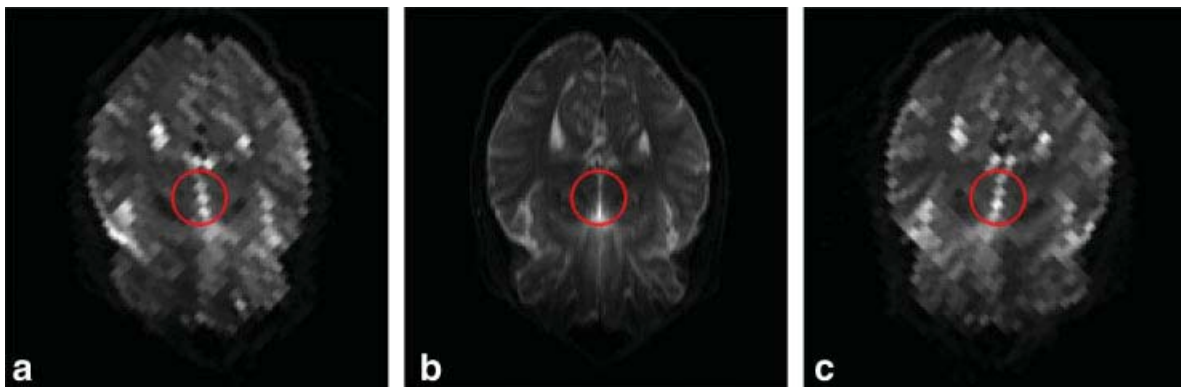


FIG. 1. Axial view of three (resampled) low resolution acquisitions ($b = 0 \text{ s/mm}^2$), acquired with different slice orientations. Some slice direction dependent distortion is visible in the red circle. [Color figure can be viewed in the online issue, which is available at wileyonlinelibrary.com.]

larger, due to the thinner slices, the SNR of a direct HR acquisition would be a factor 4 lower than the SNR of the LR images. To evaluate the method, several other datasets were constructed, representing direction acquisitions: a HR isotropic dataset ($40 \times 40 \times 40$), an isotropic LR dataset ($20 \times 20 \times 20$) and an anisotropic LR dataset ($40 \times 40 \times 10$). A noise free HR dataset ($40 \times 40 \times 40$) was generated to compare all data sets and for visualization the LR data sets were interpolated onto a $40 \times 40 \times 40$ grid using cubic spline interpolation. The power of the object signal scales linearly with the slice thickness. To simulate this, the signal of each dataset was multiplied by the ratio between its slice thickness and the HR slice thickness and the magnitude of the HR $b = 0$ s/mm² images was 1. For the anisotropic LR images and the isotropic LR image, the scaling factor was 4 and 2, respectively. Next, the DT model was fitted to the datasets, followed by calculating a direction encoded color (DEC) (26) map and applying “whole brain” tractography (27). From the whole brain tractography dataset, only the trajectories that connected one of three pairs of begin and end region of interests (ROI), which were known to be connected a priori, were selected. The proposed method reconstructs the DW images and then estimates the DT model (DW reconstruction), for comparison, the DT was estimated for each slice direction before reconstruction, followed by reconstructing the six unique DT components (DT reconstruction). To evaluate the robustness of the SRR method against noise, the standard deviation (σ) of the applied noise was varied and for each value, the SRR dataset was compared with reference datasets with an equal noise level. For visual comparison, a fixed noise level of $\sigma = 0.4$ was used.

DTI Hardware Phantom

Next, the SRR method was evaluated on a custom-made hardware DTI phantom (28). This phantom consisted of a pair of crossing fibers, a pair of kissing fibers and set of parallel fibers in a salted water-filled clear plastic spherical phantom with a diameter of 160 mm. DW data of the phantom was acquired with a Trio Scanner (3T; Siemens AG, Siemens Medical Solutions, Erlangen, Germany) with a 32-channel head coil. For the reconstruction dataset, nine datasets with different slice orientations were acquired, see Appendix for a detailed description of these orientations. As a reference, two HR sets were acquired in a single direction. The acquisitions all were multislice single-shot EPI sequences without slice gap, no averaging, in-plane resolution 1.33×1.33 mm², acquisition matrix 128×128 with 95 phase encoding steps, 100% sampling, TE = 89 ms. The FOV of all datasets was $170 \times 170 \times 166$ mm³ and each included 12 DW images ($b = 1000$ s/mm²) and 1 non-DW image ($b = 0$ s/mm²).

- The LR images for the reconstruction were acquired with slice thickness of 5.2 mm, TR = 4400 ms, pixel bandwidth 1347 Hz, and contained 32 slices. The total acquisition time for all nine slice orientations together was 8.6, min. Each of the (DW) images was reconstructed with the proposed method on a grid with 1.3 mm isotropic resolution.
- The HR datasets were acquired with slice thickness of 1.3 mm, TR = 17300 ms, pixel bandwidth 1260 Hz,

and contained 128 slices. The first HR dataset (short HR) consisted of three repetitions (36 DW and 3 $b = 0$ s/mm² images) in an acquisition time of 11.2 min. For the second reference scan (long HR), 10 repetitions were acquired (120 DW and 10 $b = 0$ s/mm² images), with a total acquisition time of 37.5 min.

Next, for each dataset the DT was estimated, followed by calculating a DEC map.

Human In Vivo Data

Finally, the reconstruction method was evaluated with human in vivo data. For this, DW data of a healthy 27-year-old male volunteer was acquired by the same Trio Scanner with a 32-channel head coil. For the reconstruction method, eight anisotropic LR DWI datasets were acquired with settings equal to the direct anisotropic LR described below. The difference in these eight datasets was the orientation of the slices, on which the SRR method is based, see Appendix. In hindsight, a smaller FOV would have been sufficient for imaging the brain.

The total acquisition time was approximately 8.8 min. The (DW)images were reconstructed by the proposed method. To evaluate the method, several additional datasets were acquired:

All datasets were acquired with a multislice single-shot EPI sequence without slice gap, no averaging, and included, unless noted otherwise, 12 DW images ($b = 1000$ s/mm²) and 1 non-DW image ($b = 0$ s/mm²).

- A direct isotropic HR dataset with 32 DW images and voxel dimensions equal to $1.5 \times 1.5 \times 1.5$ mm³, TR = 15, 100 ms, TE = 98 ms, a FOV of $255 \times 255 \times 135$ mm³, acquisition matrix 170×170 with 128 phase encoding steps, 100% sampling, 90 slices, pixel bandwidth 1471 Hz, scanning time of 8.3 min. Note that the scanning time is almost equal to the set of LR images, but the FOV is substantially smaller.
- A direct isotropic LR dataset with voxel dimensions equal to $2 \times 2 \times 2$ mm³, a TR = 7800 ms, TE = 90 ms, a FOV of $256 \times 256 \times 120$ mm³, acquisition matrix 128×128 with 102 phase encoding steps, 100% sampling, 60 slices, pixel bandwidth 1628 Hz, scanning time 1.7 min.
- A direct anisotropic LR dataset with voxel dimensions equal to $1.5 \times 3 \times 6$ mm³, a TR = 5100 ms, TE = 92 ms, a FOV of $230 \times 230 \times 240$ mm³, acquisition matrix 152×76 with 76 phase encoding steps, 100% sampling, 40 slices, pixel bandwidth 1645 Hz, scanning time of 1.1 min.

Next, for each dataset the DT was estimated, followed by calculating a DEC map and applying “whole brain” tractography. From the whole brain tractography dataset, 1000 fibers running through a midsagittal ROI of the corpus callosum were selected.

RESULTS

DTI Software Phantom

Figure 2 shows DEC maps constructed from the different datasets in all three orthogonal directions. As can be

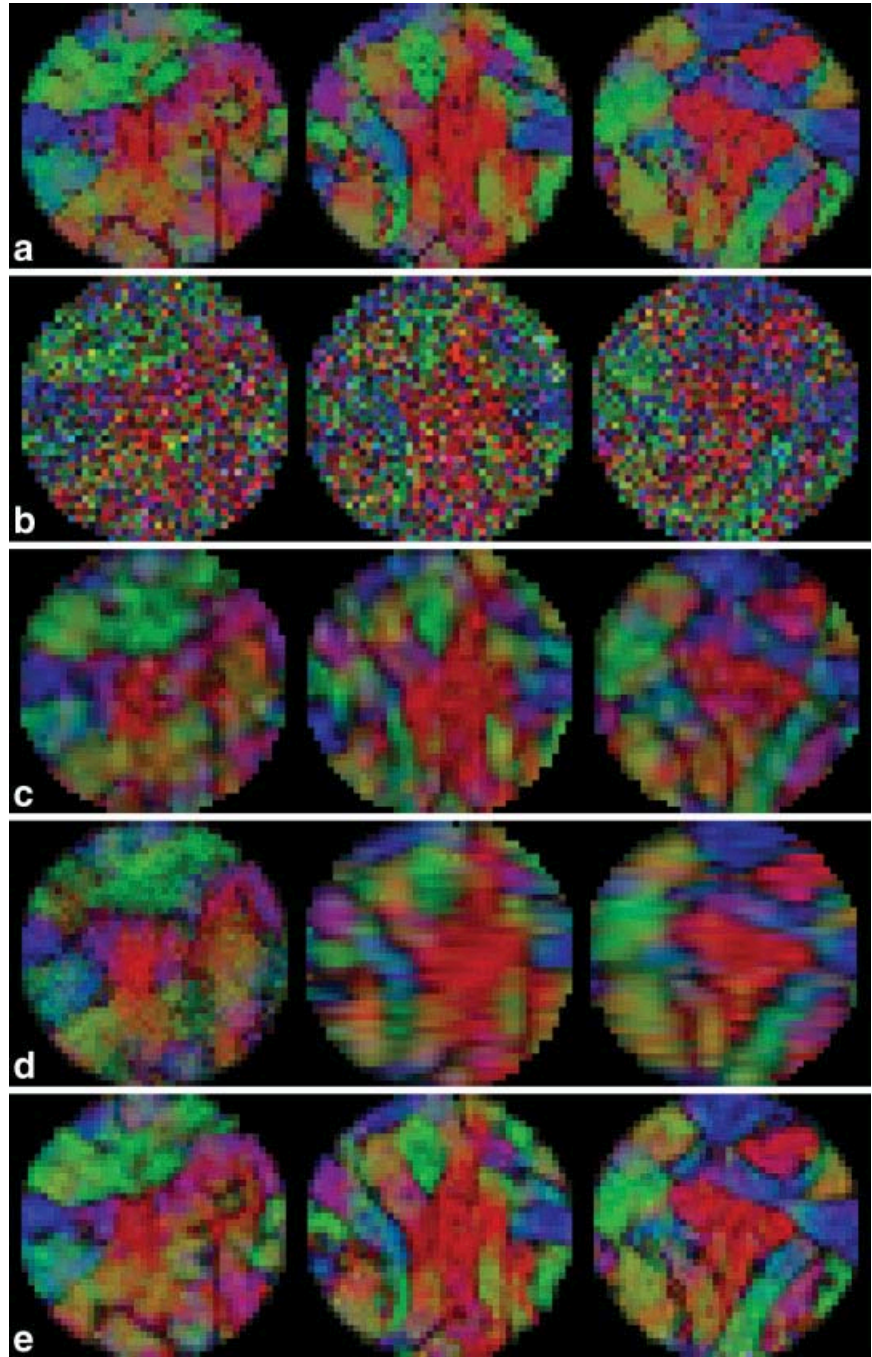


FIG. 2. Three orthogonal views of the DEC map of the simulated phantom, with directions: left – right (red), up – down (blue), back – front (green). The noise level in all noisy simulated images was $\sigma = 0.4$. (a) Original (voxels: $1 \times 1 \times 1$); (b) Isotropic HR (voxels: $1 \times 1 \times 1$, $\sigma = 0.4$); (c) Isotropic LR (voxels: $2 \times 2 \times 2$, $\sigma = 0.4$); (d) Anisotropic LR (voxels: $1 \times 1 \times 4$, $\sigma = 0.4$); (e) DW SRR (voxels: $1 \times 1 \times 1$, $\sigma = 0.4$). [Color figure can be viewed in the online issue, which is available at wileyonlinelibrary.com.]

seen, the isotropic HR dataset (Fig. 3b) suffers from a low SNR, in contrast with the anisotropic (Fig. 2d) and isotropic LR dataset (Fig. 2c). However, the isotropic LR dataset clearly shows less detail due to partial volume effects. The anisotropic LR dataset shows better resolution in one direction, but fine structures are lost in the other two directions. The SRR data (Fig. 2e), conversely, shows an improvement in details while preserving high SNR. It closely resembles the original data (Fig. 2a) except for some minor smoothing effects, mainly due to the regularization of the reconstruction.

Figure 3 shows three fiber tracts that were generated from known ROIs and computed with a “whole brain” tractography scheme. When using the isotropic HR data

(Fig. 3b), the tractography method finds substantially fewer tracts than in the original data (Fig. 3a), due to the large amount of noise. The isotropic (Fig. 3c) and anisotropic LR data (Fig. 3d) tractography schemes manage to find more fiber tracts; however, they fail in certain directions. The tractography results from the SSR dataset, conversely, closely resembles these from the original data.

The reconstruction using the DT components compared with the reconstruction of the DW images gave similar results, as can be seen in Fig. 4. However, judging from the borders of the object, the DEC map of the DT SRR suffers from more outliers than the DW SRR, due to small ringing artifacts at the borders, caused by the reconstruction.

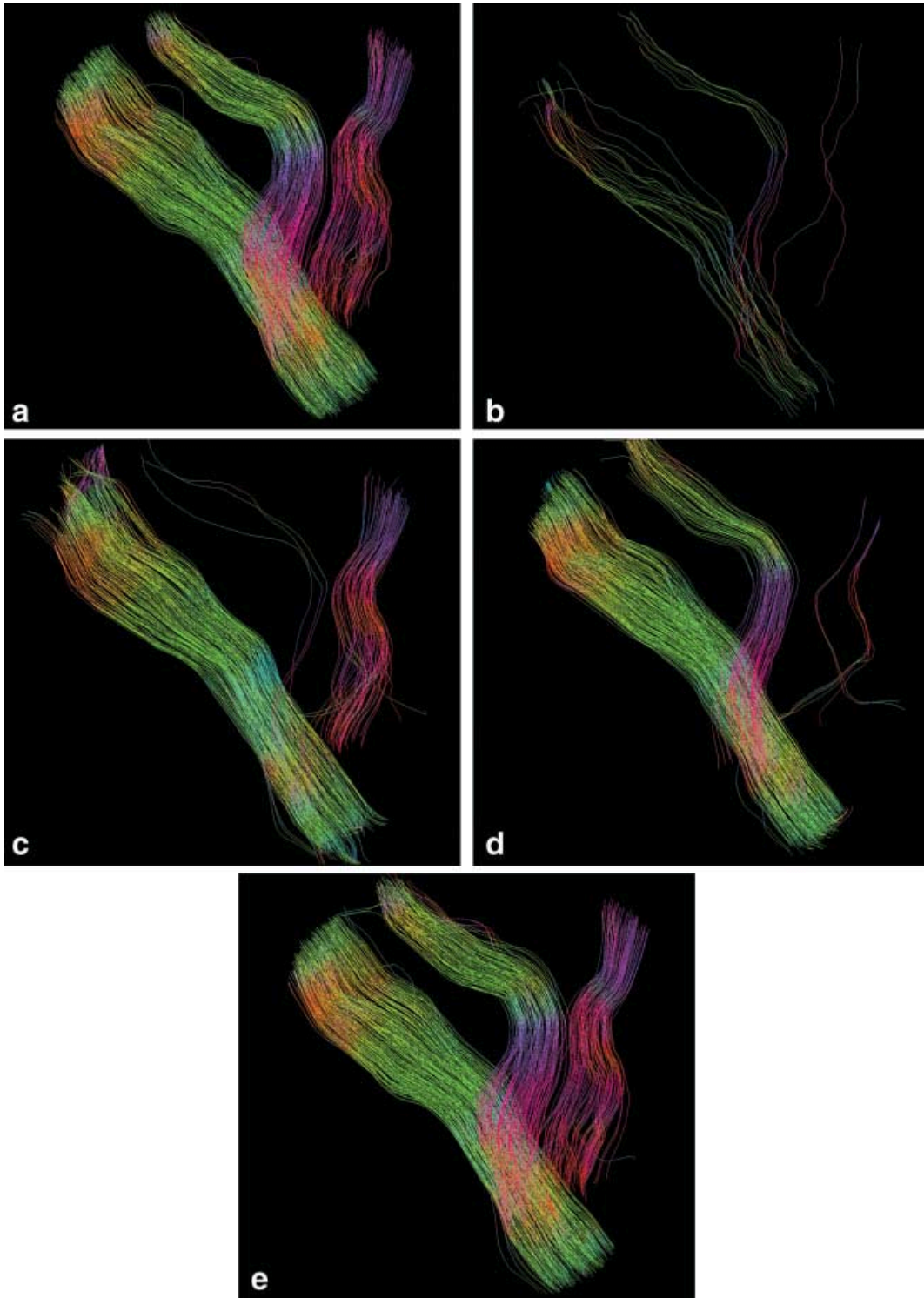


FIG. 3. “Whole brain” tractography of the simulated phantom of three different fiber tracts, with directions: left – right (red), up – down (blue), back – front (green). (a) Original (voxels: $1 \times 1 \times 1$); (b) Isotropic HR (voxels: $1 \times 1 \times 1$, σ : 0.4); (c) Isotropic LR (voxels: $2 \times 2 \times 2$, σ : 0.4); (d) Anisotropic LR (voxels: $1 \times 1 \times 4$, σ : 0.4); (e) DW SRR (voxels: $1 \times 1 \times 1$, σ : 0.4). [Color figure can be viewed in the online issue, which is available at wileyonlinelibrary.com.]

To quantify the difference in reconstruction quality, the MSE of the FA (FA-MSE), the median angular error of the FE (FE-MAE) and the SNR of the diffusion tensors were computed. The SNR (dB) was defined as:

$$\text{SNR(dB)} = 10 \log_{10} \frac{\sum_k r_0^2(k)}{\sum_k \sigma^2(r_0(k))} \quad [9]$$

with $\sigma^2(r_0(k))$ the variance of $r_0(k)$ evaluated voxelwise by performing multiple simulations with different noise

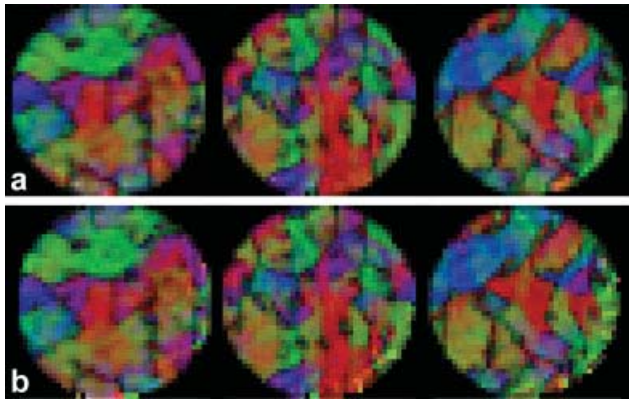


FIG. 4. DEC map comparison between the (a) DW SRR and the (b) DT SRR, with directions: left – right (red), up – down (blue), back – front (green). The same images with $\sigma = 0.4$ were used for both DEC maps. [Color figure can be viewed in the online issue, which is available at wileyonlinelibrary.com.]

realizations. Figure 5 shows the FA-MSE, FE-MAE, and SNR of the SRR and reference datasets, as a function of the noise level. The SRR data shows only a slight increase in FA-MSE (Fig. 5a) and FE-MAE (Fig. 5b) in comparison with the HR data, when increasing the noise. At a very small standard deviation of noise, the FA-MSE of the HR data is slightly below that of the DW SRR data, which is due to the small blurring effect of the SRR method. However, as can be observed from (Fig. 5c), the SNR of the SRR image is always significantly larger than that of the directly acquired HR image. The FA-MSE and FE-MAE of the isotropic and anisotropic LR images is higher due to two effects. First, for the isotropic LR data, the SNR is lower than that of the reconstructed dataset. Second, the resolution is lower, causing errors at small scale features and edges. By obtaining better resolution with a good SNR, this again demonstrates the benefits of the reconstruction method. The DW SRR is slightly better than the DT SRR, especially for the FE-MAE, due to an increased number of outliers in the DT reconstruction.

DTI Hardware Phantom

Figures 6a–c show one slice of the DEC maps of the three acquisitions. These DEC maps show that the accuracy and resolution of the reconstructed images is comparable to that of the HR acquisitions. However, the precision is improved, which can be seen from the reduced noise-induced FA in the homogenous water solution. Unfortunately, due to an acquisition artifact of which the origin is still unclear, an anomalous signal reduction was observed around the structures in images with diffusion weighting along the “green” direction. This causes the green halo around the structures. Figure 6d shows one element of the diffusion tensor (D_{xz}) along the crossing fiber visible in the DEC map (crossing around 0.5). As is clearly visible, the coefficient estimated from the reconstruction accurately traces the coefficient estimated from the long HR acquisition, without any significant bias or smoothing, and is more precise than the short HR-estimated coefficient. To investigate resolution in more detail, Fig. 6e shows the energy in spatial frequencies along lines containing uniform water. As this part is uniform,

ideally there should be no energy present after subtraction of the mean. The three diagonal and the three unique off-diagonal diffusion tensor elements are combined since the water solution is isotropic. If the reconstruction would be smoothed with respect to the direct HR acquisitions, it would contain less energy at high spatial frequencies. As this figure shows, the resolution is essentially equal for the three images. However, the noise level in the SRR dataset is approximately a factor 1.75 lower than that of the short HR data set and even a factor 1.25 lower than the long HR dataset.

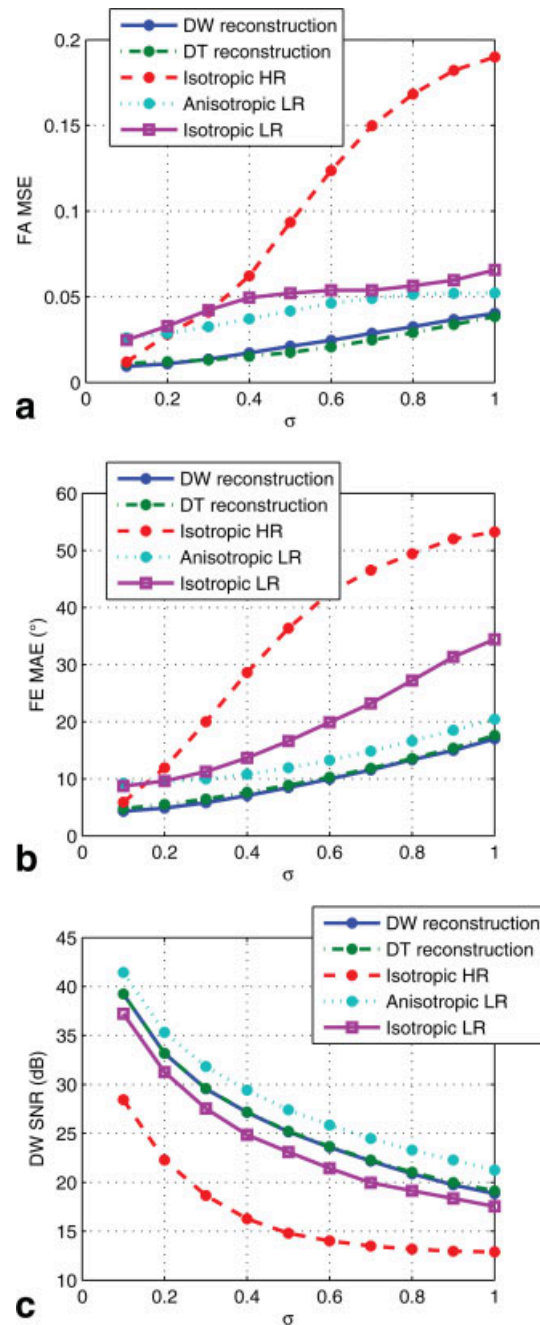


FIG. 5. The FA MSE (a), the FE MAE (b) and the DW SNR (c) of the DW SRR, DT SRR, isotropic HR, isotropic LR, and the anisotropic LR data as function of the standard deviations of noise applied to the simulated phantom. [Color figure can be viewed in the online issue, which is available at wileyonlinelibrary.com.]

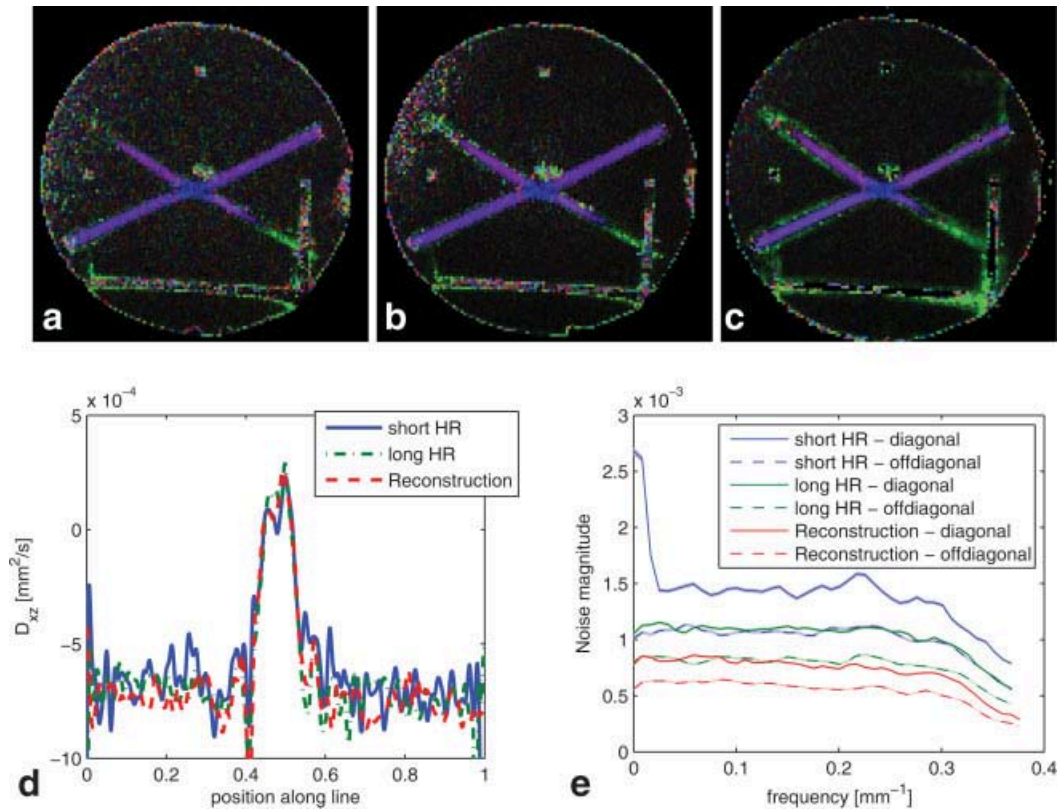


FIG. 6. DTI hardware phantom images. (a–c) show the DEC map of the short HR, long HR, and SRR datasets, respectively. This view mainly shows the isotropic water part, with two purple colored crossing fibers and some signal void regions (plastic) in which no reliable diffusion tensor can be estimated. Figure (d) shows the coefficient of the diffusion tensor that changes most in the crossing along the fiber that runs from bottom left to top right. Figure (e) shows the average spectrum of diffusion tensor elements in an isotropic water part, averaged over more than 200 lines not intersecting any structure. [Color figure can be viewed in the online issue, which is available at wileyonlinelibrary.com.]

Human In Vivo Data

Figure 7 shows DEC maps of the in vivo data. The isotropic HR data (Fig. 7a) shows fine structures but clearly suffers from a low SNR. The isotropic (Fig. 7b) and anisotropic LR data (Fig. 7c), conversely have a higher SNR but lack sufficient spatial resolution. From the DEC map of the SRR data (Fig. 7d), it can be observed that an image with a HR is reconstructed while retaining a high SNR, although, currently, outside of the brain, more voxels with erroneous high FA are present.

Figure 8 shows tractography results generated from the different datasets with the corpus callosum used as a ROI. The tractography of the isotropic HR data (Fig. 8a) clearly misses tracts in all directions in comparison with the SRR data (Fig. 8d), due to its low SNR. The anisotropic LR data (Fig. 8c) also misses tracts, due to the partial volume effects, especially in the slice direction. The tractography of the isotropic LR data (Fig. 8b) shows a large number of fiber tracts in all directions, but still misses many tracts in comparison with those from the SRR data.

For each dataset, the SNR of the $b = 0 \text{ s/mm}^2$ image was computed within the same 6 mm radius sphere located in white matter in the parietal lobe. The SNR was computed by dividing the mean signal intensity of the sphere by the noise standard deviation, which was estimated from the residue after fitting a 3D-second order polynomial (10 coefficients). The rationale for estimating the noise level

within a homogeneous part of the image, is the inhomogeneous noise profile due to the multicoil setup. Residual anatomic variability within the sphere will increase the estimated noise level and thus limit the maximum achievable SNR. The $\text{SNR}_{\text{HR}} = 10.9$, $\text{SNR}_{\text{LR}} = 20.9$, $\text{SNR}_{\text{Ani}} = 31.8$, and $\text{SNR}_{\text{SSR}} = 33.4$, for the HR, LR, anisotropic, and SSR dataset, respectively. This clearly demonstrates a substantial increase in SNR of the reconstruction dataset, compared to the HR dataset, and even when compared to the LR dataset. The SNR_{SSR} is comparable to SNR_{Ani} , one of the LR datasets.

Computational Requirements

All algorithms were written in MATLAB and partially in C++. The present implementation used an Intel i7 3.48 GHz quad core and 12 GB of memory for the reconstructions. The reconstruction of simulated DTI data with 67 images in total took 422 s, which is 6.3 s per image. The reconstruction of the human in vivo data with 13 images in total took 2230 s, which is 171 s per image. These reconstruction times can still be decreased, e.g., through GPU computing and parallel reconstruction.

DISCUSSION

DTI experiments should be optimized with respect to the conflicting requirements of good spatial resolution, fast

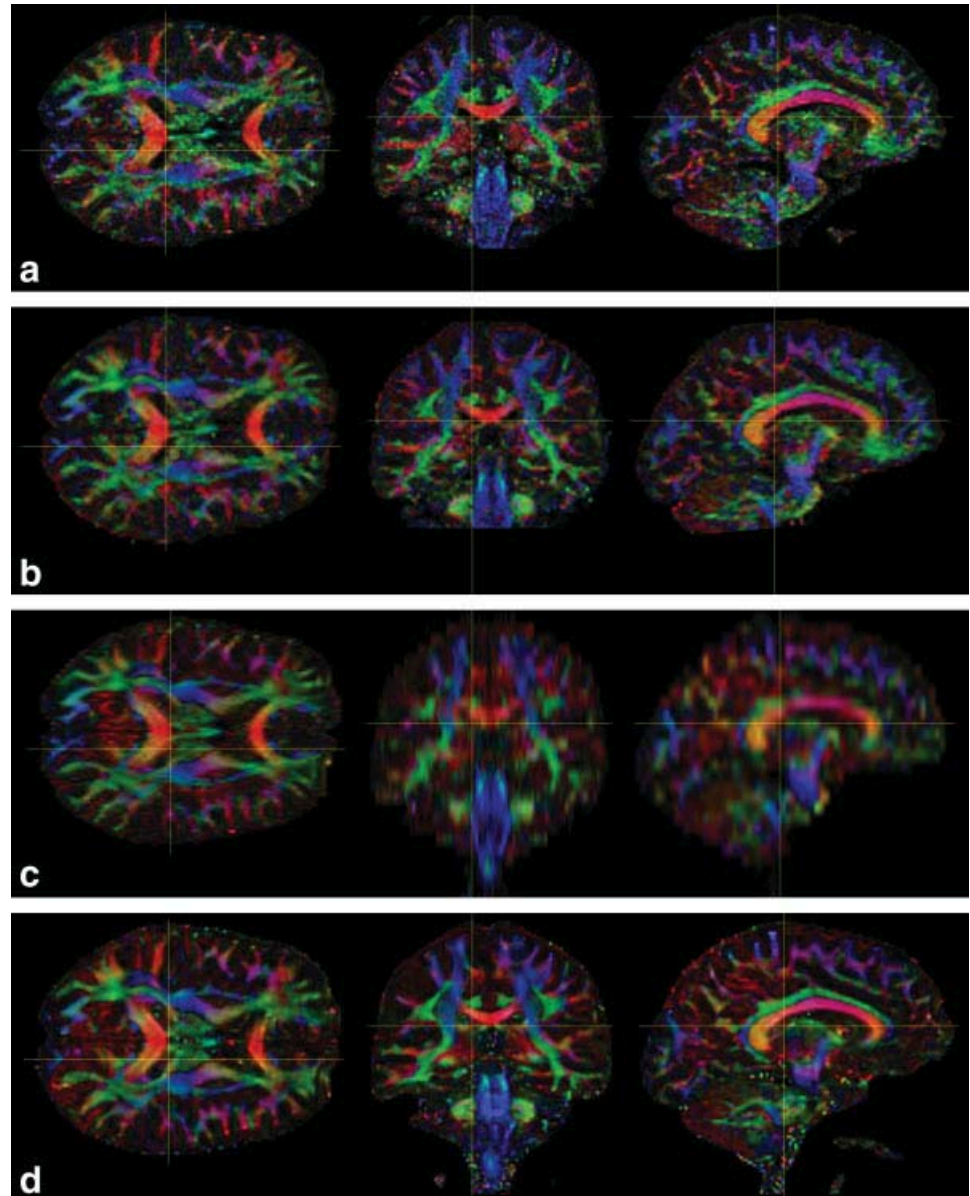


FIG. 7. Cubic interpolated DEC map of the human in vivo data, with directions: left – right (red), superior – inferior (blue), anterior – posterior (green). (a) Isotropic HR (voxels: $1.5 \times 1.5 \times 1.5 \text{ mm}^3$); (b) Isotropic LR (voxels: $2 \times 2 \times 2 \text{ mm}^3$); (c) Anisotropic LR (voxels: $1.5 \times 3 \times 6 \text{ mm}^3$); (d) DW SRR (voxels: $1.5 \times 1.5 \times 1.5 \text{ mm}^3$); Left column: axial, center column: coronal, right column: sagittal. The thin yellow lines indicate the intersections of the views.

scan time, and good SNR. In this work, a novel method was presented that achieves isotropic HR DTI data with a high SNR, within feasible scanning times. The method enables the reconstruction of HR images from a set of arbitrarily oriented low through-plane resolution images. Applied to DTI data, each DW image was reconstructed from multiple arbitrarily oriented images with a low through-plane resolution. The experiments demonstrated that HR DW images can be reconstructed with a high SNR, which in turn results in DT parameters with improved precision.

A crucial step in the proposed method is the spatial alignment of the datasets. Incorrect registration leads to blurring in the reconstruction and artifacts and image distortions that are not corrected may deteriorate the reconstructed DWI and affect the estimated diffusion tensors. The reconstruction process can be improved by adding more and/or better penalty functions to the reconstruction [e.g., based on total variation minimization (29)]. As

mentioned before, several artifacts were corrected using affine transformations. Motion correction requires the rotation component of the distortion to be incorporated in the diffusion weighting gradient (30). Unfortunately, rotation of the b-matrix is currently not supported by our method. To incorporate this, the reconstruction model would have to be extended with the DTI model, which would allow to randomly mix diffusion and slice directions and not requiring multiple slice directions per diffusion direction to be reconstructed into one DW image. This is a topic of further research. Furthermore, reconstructing the DT components instead of the DW images would have been an alternative for allowing b-matrix corrections. However, Fig. 4 shows that this causes outlier values at the borders. This is probably due to the nonlinearity in the parameters of the DTI model. As the DW SRR does not have such outliers, we suggest to use the DW SRR over the DT SSR.

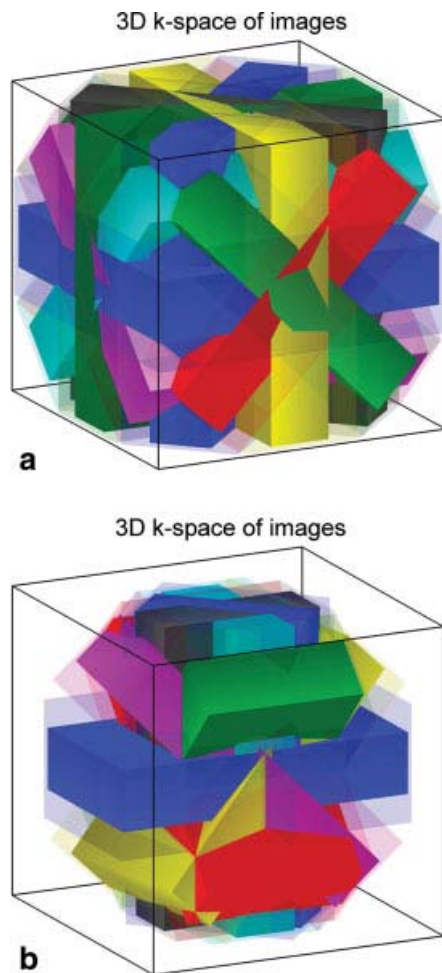


FIG. A1. Schematic visualization of the parts of 3D k -space sampled by the individual images in the multi-orientation low resolution sets. (a) Phantom dataset; (b) Volunteer dataset. [Color figure can be viewed in the online issue, which is available at wileyonlinelibrary.com.]

To fully appreciate these sampling schemes, the sampling in k -space should be studied. If 3D acquisitions would have been acquired, each image would sample inside a box in k -space. Although multislice images were acquired, they still approximately sample from within a box in 3D k -space. However, due to the slice excitation profile, there is no hard cutoff in the through plane direction. The reconstruction process can only reconstruct the parts of k -space that were sampled. Figure A1 shows the boxes of both datasets. Fig. A1 shows that most of the 3D- k -space was sampled in the phantom dataset. Unfortunately, there were substantial gaps between the boxes in the volunteer dataset. This indicates that some spatial frequencies were not sufficiently sampled to be accurately reconstructed. With 8 orientations, such large gaps can however be avoided; i.e. slightly better sets of slice orientations are still possible.

REFERENCES

1. Basser P, Mattiello J, LeBihan D. MR diffusion tensor spectroscopy and imaging. *Biophys J* 1994;66:259–267.
2. Stejskal E, Tanner J. Spin diffusion measurements: spin echoes in the presence of a time-dependent field gradient. *J Chem Physics* 1965;42:288–292.
3. Mansfield P. Real-time echo-planar imaging by NMR. *Brit Med Bull* 1984;40:187–190.
4. Mansfield P. Multi-planar image formation using NMR spin echoes. *J Physics C: Solid State Physics* 1977;10:L55–L58.
5. Turner R, Le Bihan D, Maier J, Vavrek R, Hedges L, Pekar J. Echoplanar imaging of intravoxel incoherent motion. *Radiology* 1990;177:407–414.
6. Tournier J, Mori S, Leemans A. Diffusion tensor imaging and beyond. *Magn Reson Med* 2011;65:1532–1556.
7. Tuch D, Reese T, Wiegell M, Makris N, Belliveau J, Wedeen V. High angular resolution diffusion imaging reveals intravoxel white matter fiber heterogeneity. *Magn Reson Med* 2002;48:577–582.
8. Peled S, Yeshurun Y. Superresolution in MRI: application to human white matter fiber tract visualization by diffusion tensor imaging. *Magn Reson Med* 2001;45:29–35.
9. Carmi E, Liu S, Alon N, Fiat A, Fiat D. Resolution enhancement in MRI. *Magn Reson Imaging* 2006;24:133–154.
10. Scheffler K. Superresolution in MRI? *Magn Reson Med* 2002;48:408.
11. Ropele S, Ebner F, Fazekas F, Reishofer G. Super-resolution MRI using microscopic spatial modulation of magnetization. *Magn Reson Med* 2010;64:1671–1675.
12. Greenspan H, Oz G, Kiryati N, Peled S. MRI inter-slice reconstruction using super-resolution. *Magn Reson Imaging* 2002;20:437–446.
13. Kornprobst P, Peeters R, Nikolova M, Deriche R, Ng M, Hecke P. A super-resolution framework for fMRI sequences and its impact on resulting activation maps. *Medical Image Computing and Computer-Assisted Intervention - MICCAI 2003*. Vol. 2 New York: Springer 2003;117–125.
14. Gholipour A, Estroff J, Warfield S. Robust super-resolution volume reconstruction from slice acquisitions: application to fetal brain MRI. *IEEE Trans Med Imaging* 2010;29:1739–1758.
15. Rousseau F, Glenn O, Iordanova B, Rodriguez-Carranza C, Vigneron D, Barkovich J, Studholme C. Registration-based approach for reconstruction of high-resolution in utero fetal MR brain images. *Acad Radiol* 2006;13:1072–1081.
16. Shilling R, Robbie T, Bailloleul T, Mewes K, Mersereau R, Brummer M. A super-resolution framework for 3-D high-resolution and high-contrast imaging using 2-D multislice MRI. *IEEE Trans Med Imaging* 2009;28:633–644.
17. Poot D, Van Meir V, Sijbers J. General and efficient super-resolution method for multi-slice MRI. *MICCAI 2010*;13:615–622.
18. Jiang Y, Hsu E. Accelerating MR diffusion tensor imaging via filtered reduced-encoding projection-reconstruction. *Magn Reson Med* 2005;53:93–102.
19. Nunes RG, Jezzard P, Behrens TEJ, Clare S. Self-navigated multishot echo-planar pulse sequence for high-resolution diffusion-weighted imaging. *Magn Reson Med* 2005;53:1474–1478.
20. Sijbers J, den Dekker AJ, Scheunders P, Van Dyck D. Maximum likelihood estimation of Rician distribution parameters. *IEEE Trans Med Imaging* 1998;17:357–361.
21. Pruessmann KP, Weiger M, Scheidegger MB, Boesiger P. SENSE: sensitivity encoding for fast MRI. *Magn Reson Med* 1999;42:952–962.
22. Sodickson DK, Manning W. Simultaneous acquisition of spatial harmonics (SMASH): fast imaging with radiofrequency coil arrays. *Magn Reson Med* 1997;38:591–603.
23. Hestenes M, Stiefel E. Methods of conjugate gradients for solving linear systems. *J Res Nat Bur Stand* 1952;49:409–436.
24. Close T, Tournier J, Calamante F, Johnston L, Mareels I, Connelly A. A software tool to generate simulated white matter structures for the assessment of fibre-tracking algorithms. *Neuro Image* 2009;47:1288–1300.
25. Jones D, Horsfield M, Simmons A. Optimal strategies for measuring diffusion in anisotropic systems by magnetic resonance imaging. *Magn Reson Med* 1999;42:515–525.
26. Pajevic S, Pierpaoli C. Color schemes to represent the orientation of anisotropic tissues from diffusion tensor data: application to white matter fiber tract mapping in the human brain. *Magn Reson Med* 1999;42:526–540.
27. Basser P, Pajevic S, Pierpaoli C, Duda J, Aldroubi A. In vivo fiber tractography using DT-MRI data. *Magn Reson Med* 2000;44:625–632.
28. Pullens P, Roebroek A, Goebel R. Ground truth hardware phantoms for validation of diffusion-weighted MRI applications. *J Magn Reson Imaging* 2010;32:482–488.
29. Block K, Uecker M, Frahm J. Undersampled radial MRI with multiple coils. iterative image reconstruction using a total variation constraint. *Magn Reson Med* 2007;57:1086–1098.
30. Jones D, Cercignani M. Twenty-five pitfalls in the analysis of diffusion MRI data. *NMR biomed* 2010;23:803–820.